PFC/JA-90-1

Possible Achievement of Second Stability
by Means of Lower Hybrid Current Drive

P. T. Bonoli, M. Porkolab, J. Ramos,
D.T. Blackfield*, R.S. Devoto† and M.E. Fenstermacher†

Plasma Fusion Center
Massachusetts Institute of Technology
Cambridge, MA 02139

October, 1989

* TRW, Redondo Beach, CA 90278 (LLNL, Livermore, CA 94550).

† LLNL, Livermore, CA 94550.

Possible Achievement of Second Stability
by Means of Lower Hybrid Current Drive

P. T. Bonoli, M. Porkolab, and J. J. Ramos
PLASMA FUSION CENTER, MIT, Cambridge, MA 02139
D. T. Blackfield*
TRW, Redondo Beach, CA 90278
R. S. Devoto and M. E. Fenstermacher
LLNL, Livermore, CA 94550

Abstract

It is shown that radial profiles of the safety factor $q(r)$, necessary to access the so-called "second stability" regime in shaped, low aspect ratio tokamaks, can be achieved via off-axis lower hybrid current drive (LHCD). In order to accurately model the required current profiles, our previous simulation code for LHCD has been extended to noncircular equilibria and combined with an MHD equilibrium solver. As a particular example, results will be presented for Versator Upgrade tokamak parameters.

*Present Address: Lawrence Livermore National Laboratory, Livermore, CA 94550

I. Introduction

It has been shown [1,2] that for low aspect ratio ($R_o/a = 3$) shaped, tokamak equilibria with safety factor in the range $2 \gtrsim q(\psi) \gtrsim 8$, a sequence of MHD equilibria exist which allow a stable path to a high beta operating regime. Access to this region of the so-called "second stability regime" would greatly improve the operating space for D-T fusion reactors, and would allow operation with advanced fuels such as $D - ^3He$ [3]. Furthermore, it would make steady state reactor operation more attractive owing to an increase in the bootstrap current at high values of $\epsilon\beta_p$. In this paper, it is shown that the required $q(\psi)$ profiles, in particular $q_o > 1$, can be achieved via off-axis lower hybrid current drive (LHCD). Specifically, it is shown that for parameters characteristic of the entrance to the second stability regime in the proposed Versator Upgrade device [4] [$R_o/a = 3$, elongation $\kappa = 1.4$, triangularity $\delta = 0.3$, $n_{eo} = 3 \times 10^{19} m^{-3}$, $B_\phi = 1$ T, $I_p = 150$ kA, $T_{eo} \simeq T_{io} \gtrsim 2$ keV], the required profiles of the safety factor with $q_o \gtrsim 2$, $q(a) \simeq 8$, $q_o \gtrsim q(\psi) \gtrsim q(a)$, can easily be achieved via LHRF current generation combined with ohmic currents. The required RF power is $P_{LH} \gtrsim 0.3$MW at $f_o = 2.45$ GHz for combined ohmic-LHRF scenarios with $I_{RF} \simeq 70$ kA and $I_{OH} \simeq 80$ kA. If bootstrap current generation is also included, the RF power requirement is reduced to $P_{LH} \simeq 0.15$ MW with $I_{BS} \simeq 75$ kA, $I_{OH} \simeq 40$ kA, and $I_{RF} \simeq 35$ kA. The level of bootstrap current generated in the presence of LHRF is significantly enhanced relative to combined ohmic-bootstrap current generation alone, where $I_{BS} \simeq 45$ kA and $I_{OH} \simeq 105$ kA. A stability analysis of these results indicates the calculated $q(\psi)$ profiles are stable to both high-n and low-n ideal MHD, ballooning modes (where n is the toroidal mode number). These results can easily be extended for a completely RF driven operation using additional RF systems and antennas, and for combined neutral beam injection(NBI)-RF systems for steady state reactor operation in the second stability regime. In order to accurately model this RF current generation, our previous LHCD simulation model [5] has been modified for noncircular equilibria and added to a code which self-consistently computes free or fixed boundary MHD equilibria [6] and current generated by neutral beams [7], ohmic electric fields and bootstrap effects [8,9].

The plan of this paper is as follows. The combined MHD solver and LHCD package is described in Sec. II, model results are presented in Sec. III, and conclusions are given in Sec. IV.

II. Model Calculation

Free boundary MHD equilibria are obtained by solving the Grad-Shafranov equation [10] using a source term which includes ohmic (J_{OH}), lower hybrid (J_{RF}), bootstrap (J_{BS}), and neutral beam (J_{NB}) driven currents:

$$\Delta^*\psi = -\mu_o R^2 \frac{d}{d\psi}p(\psi) - F(\psi)\frac{dF(\psi)}{d\psi}, \tag{1a}$$

$$\Delta^*\psi \equiv R\frac{\partial}{\partial R}\left(\frac{1}{R}\frac{\partial\psi}{\partial R}\right) + \frac{\partial^2\psi}{\partial z^2}, \tag{1b}$$

$$F\frac{dF}{d\psi} = -\mu_o \left[F^2\frac{d}{d\psi}p(\psi) + F\langle J_{\parallel}B\rangle\right] / \langle B^2\rangle. \tag{1c}$$

Here, ψ is the poloidal flux function, $F = RB_t$ is the toroidal function, B_t is the toroidal magnetic field, $R\underline{B} = \underline{\nabla}\psi \times \underline{e}_\phi + F\underline{e}_\phi$, $p(\psi)$ is a specified pressure profile, $\langle\rangle$ denotes a flux surface average, $R = (x^2 + y^2)^{1/2}$ is the major radial position (measured in the equatorial plane of the tokamak), and $J_{\parallel} = J_{OH} + J_{RF} + J_{BS} + J_{NB}$ is the total current density (along $\underline{B}$). In the present work only the ohmic, bootstrap, and LHRF current densities are considered (i.e., $J_{NB} = 0$). The iteration procedure used to solve Eq. (1) is started by first assuming that $J_{RF} = 0$ and the plasma current is purely ohmic, i.e., $J_{OH} = E_{\parallel}/\eta_{\parallel}$ and $E_{\parallel}$ is adjusted so that the total plasma current $I_p = \int J_{\parallel}(\psi)dA(\psi)$ is equal to a specified value. Equation (1) is then solved to obtain a first approximation to the MHD equilibrium and the LHRF current is calculated based on this new MHD equilibrium. $E_{\parallel}$ is again adjusted to keep I_p constant and the Grad-Shafranov equation is solved a second time using the new source term. This process is repeated until the MHD equilibrium and J_{RF} no longer change. Typically, five to ten iterations between the MHD solver and the LHCD code are required in order to obtain convergence.

The LHCD package has been described in detail in Ref. 5. The calculation has been extended to noncircular geometry by integrating the ray equations in cartesian geometry,

$$\frac{dx}{dt} = -\frac{\partial\epsilon/\partial\underline{k}}{\partial\epsilon/\partial\omega}, \tag{2a}$$

$$\frac{d\underline{k}}{dt} = +\frac{\partial\epsilon/\partial\underline{x}}{\partial\epsilon/\partial\omega}, \tag{2b}$$

where $\underline{x} = (x,y,z)$, $\underline{k} = (k_x, k_y, k_z)$, (x,y) lie in the equatorial plane of the tokamak, and z is perpendicular to the equatorial plane. The LH dispersion relation $[\epsilon(\underline{x},\underline{k},\omega) = 0]$ includes electromagnetic and thermal effects. The plasma quantities, $n_e(\psi)$, $T_e(\psi)$, $T_i(\psi)$, $\underline{B}(R, \psi)$ and their spatial derivatives are given in cartesian coordinates by a bi-cubic spline interpolation of the equilibrium results of the MHD solver.

A parallel velocity Fokker Planck calculation [5] is carried out on each ψ surface in the plasma (where ψ labels a magnetic surface). The calculation is relativistically correct (i.e., $p_{\parallel} = \gamma m_e v_{\parallel}$), includes the effect of finite electron tail confinement (τ_L), an effective perpendicular electron temperature due to pitch angle scattering ($T_\perp \geq T_e$), but ignores the effect of the parallel DC electric field ($E_{\parallel}$). The quasilinear diffusion coefficient due to the RF waves, $D_{RF}(p_{\parallel},\psi)$ is consistent with the local wave amplitude and spatial damping rates. In the calculations presented here, we assume $T_\perp \cong 5 \times T_e$ (following Ref. 11), $\tau_L = \tau_o\gamma^3$, and $\tau_o \sim \tau_E \sim 8.1$ ms for the parameters given below.

III. Model Results

The parameters used to study LHRF current profile control are typical of the proposed Versator Upgrade device [4] where $a = 0.3$ m, $R_o = 0.9$ m, $B_{to} = 1.0$ T, $I_p = 150$ kA, $\kappa = 1.4$, $\delta = 0.25$, $Z_{eff} = 1.5$, hydrogen gas, $n_{eo} = 3 \times 10^{19}$m^{-3}, and $T_{eo} = T_{io} = 2.0$ keV.

The plasma profiles were chosen to be $n_e(\psi) = n_{eo}(1 - \hat{\psi})^{\gamma_n}$, $T_\alpha(\psi) = T_{\alpha o}(1 - \hat{\psi})^{\gamma_{t\alpha}}$, $\gamma_n = 1.0$, $\gamma_{te} = \gamma_{ti} = 1.25$, $\hat{\psi} = (\psi - \psi_o)/(\psi_a - \psi_o)$, ψ_a is the value of ψ on the outermost flux surface, and ψ_o is the value of ψ at the magnetic axis. The pressure profile is determined from $p(\psi) = n_e(\psi)[T_e(\psi) + T_i(\psi)]$. The frequency of the LHRF power is $f_o = 2.45$ GHz, and the relevant parameters for LH wave accessibility at the plasma center are $(\omega_{pe}/\omega_{ce})^2 = 3.09$ and $n_{\|acc} = 3.73$. Here $n_{\|acc}$ is the minimum value of parallel refractive index required for wave accessibility to the plasma center.

The RF power spectrum is assumed to have the form

$$
\begin{aligned}
S(n_\|) &= S_A \exp[-(n_\| - n_A)^2/(\Delta n_A)^2] \\
&+ S_B \exp[-(n_\| - n_B)^2/(\Delta n_B)^2] \quad , \qquad n_\| > 0 , \\
&= 0 \qquad\qquad\qquad\qquad\qquad\qquad , \qquad n_\| < 0 .
\end{aligned}
\tag{3}
$$

In the model calculations presented in this paper, it is assumed that $S_A=1.0$, $n_A=3.0$, $\Delta n_A=1.41$, $S_B=0.1$, $n_B=6.0$, and $\Delta n_B=1.0$. A sketch of $S(n_\|)$ for these parameters is shown in Fig. 1. In practice, this type of broad RF power spectrum could be produced by either superposing the spectra of two or more waveguide arrays, each phased differently, or by electronically 'sweeping' the phase of a single waveguide array. The power spectrum shown in Fig. 1 is represented on a numerical $n_\|$ grid by sixty contiguous 'bars' of power, each of width $\Delta n_\|^o=0.1$, in the range $2 \leq n_\|^o \leq 8.0$. Two different RF launcher configurations are considered. In the first configuration, a single launcher is placed at a vertical position of $z_o=25$ cm above the midplane of the torus. In the second configuration, three launchers are located at $z_o=(0, 12.5, 25)$ cm above the torus midplane (i.e., distributed launch).

A. Model Results For A Single Launcher

(i) Combined Ohmic and LHRF Currents

The results of an RF power scan using the single launcher configuration are given in Table I. In each case, the ohmic plus LHRF current totals 150 kA and the profiles of $q(\psi)$ are monotonically increasing functions of $\hat{\psi}$, in the range $0 \leq \hat{\psi} \leq 1$. The values of the current drive figure of merit in Table I are defined as $\eta_{CD}(A/W/m^2) = < n_e(10^{20}m^{-3}) >_v \times I_{RF}(kA)R_o(m)/P_{LH}(kW)$, where $<>_v$ denotes a volume average. The values of $\epsilon\beta_p$ are defined in terms of the volume average poloidal beta, $\beta_p = < p(\psi) >_v /(< B_\theta >^2 /2\mu_o)$, with $\epsilon = a/R_o$. Bootstrap currents are not included in Table I.

Approximately (75-80)% of the injected RF power is absorbed due to resonant electron Landau damping in these cases. The remaining RF power in the launched spectrum at $2 \gtrsim n_\|^o \gtrsim 3$ is not accessible to the plasma core, even after multiple radial reflections at the plasma edge (recall that $n_{\|acc} \cong 3.7$ at the plasma center). It is interesting to note that the fraction of the injected RF power lost due to electron tail losses (P_L) is negligible in all cases ($P_L \gtrsim 0.04 P_{LH}$). This small tail loss is consistent with the rapid thermalization and negligible spatial diffusion of fast electrons. Finally, the case in Table I for which $q_o \gtrsim 2$, corresponds to $\epsilon\beta_p \simeq 0.48$, a value which is quite close to the critical value of $\epsilon\beta_p \gtrsim 0.5$

3

reported in Ref. 2, for which further increases in beta would result in entering the second stability regime.

Details of the 250 kW case in Table I are shown in Figs. 2-4. Figure 2(a) is a plot of $J_{OH}(\psi)$, $J_{RF}(\psi)$, and $J_{||}(\psi)$ after the tenth and final iteration between the current drive package and the MHD equilibrium solver. The LHRF current is 67 kA and the ohmic current is 83 kA. The broad nature of the RF current density profile ($0 \gtrsim \hat{\psi} \gtrsim 0.7$) tends to broaden the total current profile, resulting in a decrease in the current density on-axis $[J_{||}(0)]$, for a fixed total current (I_p). This results in a large increase in q_o relative to the ohmic q_o as shown in Fig. 2(b). The key to producing such broad profiles of LHRF current density was found to be the use of broad RF power spectra - like that shown in Fig. 1.

The poloidal projection of a single ray trajectory (initial $n_{||}^o=3.0$) for this case is shown in Fig. 3(a). Each circular mark along the ray path indicates a 20% decrease in the wave power due to quasilinear electron Landau damping. The parallel refractive index ($n_{||}$) of the ray shown in Fig. 3(a) increased from an initial value of 3.0 to 3.8. This increase in $n_{||}$ is due to the launch of the wave from above the midplane and is a toroidal geometry effect [12]. The electron distribution function on a flux surface near the maximum in the RF deposition profile ($\hat{\psi} \simeq 0.28$) is shown in Fig. 3(b), plotted as a function of parallel kinetic energy $E=m_e c^2[n_{||}/(n_{||}^2 - 1)^{1/2}-1]$. The slowing down time for the fast electrons in the plateau region is approximately $\tau_S \gtrsim 2 \times 10^{-3}$ sec. (assuming $n_e \simeq 2.2 \times 10^{19} m^{-3}$ and $E \simeq 30$ keV at $\hat{\psi} \simeq 0.28$). However, $\tau_S \ll \tau_L$ so that fast electrons would be expected to thermalize before diffusing an appreciable distance.

In order to illustrate the importance of iterating between the MHD equilibrium solver and the lower hybrid current drive package, the results for LH wave propagation, absorption, $J(\psi)$, and $q(\psi)$ are shown in Fig. 4, after only the first iteration. Thus, the results for wave propagation and absorption were obtained for an initial ohmic plasma with $\kappa=1.40$. $\delta=0.3$, $I_p=I_{OH}=150$ kA, $I_{RF}=0$ kA, $R_o/a=3$, $q_a=7.6$, $q_o \simeq 1.0$, and $\epsilon\beta_p=1.19$. Figure 4(a) indicates that the wave absorption is stronger along the initial ray path into the plasma, relative to the tenth iteration result shown in Fig. 3(a). The stronger absorption is due to a more rapid increase of $n_{||}$ along the ray path (initial $n_{||}^o=3.0$ and final $n_{||} \simeq 4.6$), which is an equilibrium dependent toroidal effect [12]. The resulting profiles of $J_{OH}(\psi)$, $J_{RF}(\psi)$, and $q(\psi)$ after the first iteration, are shown in Figs. 4(b)-4(c), where $I_{RF}=75$ kA, $I_{OH} = 75$ kA, and $P_{abs} = 217$ kW. Although $q_o \cong 2.67$ after the first iteration, the $q(\psi)$ profile in Fig. 4(c) is multi-valued and is susceptible to a "double tearing" instability [13]. Thus, it is important to iterate between the MHD equilibrium solver and the LHRF current drive package since equilibrium variations will affect RF current generation and changes in $J_{RF}(\psi)$ will affect the equilibrium solution.

(ii) Combined Ohmic, LHRF, and Bootstrap Currents

The relatively high values of $\epsilon\beta_p$ reported in the previous section suggest that the so-called bootstrap current [14] may be important in these discharges. The LHCD and MHD equilibrium solutions have been re-calculated with bootstrap current included, for the case shown in Fig. 2 (i.e., single launcher positioned 25 cm above the midplane).

The RF power spectrum in Fig. 1 was used with $P_{LH}=130$ kW and the results after ten iterations are shown in Fig. 5. The large reduction in RF power was possible because of the significant level of bootstrap current ($I_{BS}=77$ kA, $I_{RF}=30$ kA, and $I_{OH}=43$ kA). The profile of $J_{RF}(\psi)$ in Fig. 5(a) is again broad and the total current density profile is further broadened by the bootstrap current density. The total RF power absorbed was 93 kW and $\epsilon\beta_p=0.48$. The $q(\psi)$ profile shown by the solid curve in Fig. 5(b) is a monotonically increasing function of $\hat{\psi}$ with $q_o \simeq 2.26$. The $q(\psi)$ profile in the presence of combined ohmic and bootstrap currents alone is shown by the dashed line in Fig. 5(b), with $q_o \simeq 0.81$. Without LHRF, the bootstrap current is only 47 kA ($I_{OH}=103$ kA) and $\epsilon\beta_p=0.35$. Thus, the bootstrap current is enhanced by the presence of the LHRF due to an increase in $\epsilon\beta_p$. (The enhancement in I_{BS}/I_p is due in part to the increae in β_p and also to the flattening of the current density profile.

B. Model Results For Multiple Launchers

The results of LHRF current profile control using a multiple launcher configuration and including the effect of bootstrap current are shown in Fig. 6. Radio-frequency power was injected from $z_o=(0, 12.5, 25)$ cm above the torus midplane with $P_{LH} = (40, 40, 80)$ kW, respectively, for a total of 160 kW of injected power. The same RF power spectrum (shown in Fig. 1) was used for each launcher. The total absorbed power was 103 kW with $I_{BS} = 74$ kA, $I_{RF}=35$ kA, $I_{OH} = 41$ kA, and $\epsilon\beta_p=0.47$, after the tenth iteration between the current drive and equilibrium codes. The resulting current density profiles are again rather broad and the $q(\psi)$ profile is monotonically increasing with $q_o=2.03$ [see Figs. 6(a)-6(b)]. A single ray trajectory from each of the three launch positions is shown in Fig. 6(c). The initial values of $n_{\parallel}^o$ are (5.0, 4.0, 3.0) for the rays launched at $z_o=(0, 12.5, 25)$ cm, respectively. Again, each circular mark along a ray path indicates a 20% decrease in the wave power due to quasilinear electron Landau damping.

C. Stability Calculations

The equilibrium described in Sec. IIIB and shown in Fig. 6 (combined ohmic, LHRF, and bootstrap currents), has been tested for ideal MHD stability using the PEST code package [15]. In order to carry out this anlaysis, we use the fixed boundary PEST equilibrium solver to generate a solution that matches the equilibrium obtained with the LHCD-free boundary equilibrium code. This fixed boundary PEST equilibrium is fed into the PEST stability codes. The PEST equilibrium is defined by a fixed boundary that agrees with the parameters of the plasma limiter magnetic surface ($R_o = 0.90$m, $a = 0.30$m, $\kappa = 1.4$, $\delta = 0.25$), a pressure profile identical to the one used in the current drive, free boundary calculation,

$$p(\hat{\psi}) = 1.92 \times 10^4 (1 - \hat{\psi})^{2.25} \quad \text{newton/m}^2 ,$$

and a rotational transform profile given by the following five-parameter analytical fit to the free boundary numerical output (Fig. 6b):

$$q(\hat{\psi}) = 2.03 + 3.90\hat{\psi}^3 + 1.60\hat{\psi}^{13}.$$

5

A comparison of the basic plasma parameters obtained with the two equilibrium solvers is given in Table II.

This equilibrium is found to be stable against n = ∞ Mercier and ballooning modes. Low-n external modes up to n=3 have also been tested. The n=2 and n=3 modes are stable in the absence of any conducting wall, whereas the n=1 mode is stable if a conducting wall is placed at a distance from the plasma edge equal to 0.5 times the minor radius.

The characteristic beta parameters of our equilibrium, namely $\epsilon\beta_p = 0.5$ and a Troyon ratio $\beta_T \equiv 10^8\beta(aB/I)_{MKS} = 2.4$ correspond to the upper limit of the MHD "first stability region" and the beginning of the transition to the "second stability region". This particular equilibrium has a rather peaked p-profile and flat central q-profile. For this kind of profile, access to the second stability region for the conventional n=∞ ballooning modes is easily achieved by further peaking the p-profile and flattening the q-profile as beta is increased, which pushes the equilibrium parameters into the high-α, low-s region of the ballooning stability diagram [1]. An instability-free connection between the first and second stability regimes is made possible by our high q (q > 2) values. However, this route leads to low or intermediate-n "infernal" instabilities [16] at some critical beta. In any case, the critical beta for the onset of infernal instabilities is rather high for our q > 2 configurations, since these modes are reminiscent of the global interchanges [17] whose stability is determined by the Mercier criterion. We have verified this by studying a sequence of peaked-p, flat-q equilibria that starts at our current drive equilibrium with $\epsilon\beta_p = 0.5$ and $\beta_T = 2.4$, and goes into the second stability region for n = ∞ ballooning modes. We find this sequence to be stable against all-n ideal MHD internal modes up to $\epsilon\beta_p > 0.8$, $\beta_T > 4.0$ and central beta $\beta_o > 14\%$. The onset of low-n (infernal) instabilities with the typical signature of oscillating growth rates as a function of the toroidal mode number n is observed at some $\beta_T < 4.8$. This coincides roughly with the violation of the Mercier criterion in the center of the plasma. In order to avoid the infernal instabilities, and to produce stable equilibria against all-n modes in the second regime, higher-shear and/or flatter-pressure profiles such as those considered in Ref. 2 must be adopted. In principle, such profiles can be achieved with a more elaborate phase control scenario of lower hybrid couplers than that adopted here. We shall undertake such studies in the future.

IV. Conclusions

In conclusion, a powerful computational tool has been developed to study lower hybrid current profile control in self-consistent MHD equilibria. Utilizing this model, it has been shown that the $q(\psi)$ profiles [$2 \gtrsim q(\psi) \gtrsim 8$] necessary to access a high poloidal beta operating regime ("second stability regime") in shaped tokamak equilibria can be achieved, via off-axis LHRF current generation with $I_{RF} \gtrsim 0.5 \times I_p$. It was also shown that these profiles of $q(\psi)$ were stable to both high-n and low-n (n ≤ 3) ballooning modes in the ideal MHD limit.

Several effects should be pointed out which could change the profiles of $q(\psi)$ that have been obtained. First, any variations in temperature and density which occur as the plasma is heated will change $p(\psi)$ and consequently the MHD equilibrium. Equilibrium variations

6

will affect the LHRF power deposition and current generation causing $J_{||}(\psi)$ and $q(\psi)$ to be different. Second, although the spatial diffusion of fast electrons is expected to be negligible, if any anomalous diffusion of the suprathermal current does occur, the resulting profiles of $J_{||}(\psi)$ and $q(\psi)$ would again be different. Finally, the RF power spectrum used in these calculations is idealized in the sense that $S(n_{||} < 0) = 0$. In general, this is not true and some small fraction of RF power will be launched at $v_{||} < 0$, generating negative current, which will affect the profiles of RF current density.

Finally, it should be emphasized that this model can also be used to study current profile control and steady state operation with neutral beam injection, LH current drive, and bootstrap current generation in reactor relevant plasma regimes ($n_e \gtrsim 1 \times 10^{20} m^{-3}$ and $T_e, T_i \gtrsim 25$ keV).

Acknowledgements

Table I:
q_o Versus LHRF Power
LHCD Parameters for Single Launcher Configuration

P_{LH}(kW)	q_o	$\epsilon\beta_p$	I_{RF}(kA)	η_{CD}
0	0.95	0.36	0	–
100	1.28	0.41	24.5	0.026
150	1.56	0.44	38.0	0.028
250	2.06	0.48	67.1	0.031

Table II:
Comparison of Equilibrium Parameters Obtained With the Two
Equilibrium Codes Used to Analyze Our Current Drive Configuration

	I(kA)	β	β_p	l_i
LHCD-free-boundary equilibrium code	150	1.21%	1.55	1.06
PEST-fixed-boundary equilibrium code	151	1.21%	1.56	1.07

8

References

[1] Coppi, B., Crew, G. B., Ramos, J. J., Comments Plasma Phys. Contr. Fusion 6 (1981) 109.

[2] Gerver, M. J., Kesner, J., Ramos, J. J., Phys. Fluids 31 (1988) 2674.

[3] Atzeni, S. and Coppi, B., Comments Plasma Phys. Cont. Fusion 6 (1980) 77.

[4] Porkolab, M. Bonoli, P., Chen, K. I., Coda, S., Gerver, M., et al, 12th Int. Conf. on Plasma Physics and Controlled Fusion Research (Nice, France, 1988) Paper IAEA CN-50/E-4-8.

[5] Bonoli, P. T., Englade, R. C., Phys. Fluids 29 (1986) 2937.

[6] Azumi, M., Kurita, G., Proc. 4th Int. Symp. Computing Methods in Appl. Science and Eng. (Paris, 1979) 335.

[7] Tani, K., Suzuki, M., Yamamoto, S., Azumi, M., "On The Analysis of Beam Driven Current in a Tokamak", JAERI-M 88-042 (1988).

[8] Tani, K., Azumi, M., Devoto, R. S., Journal of Computational Physics, submitted for publication.

[9] Devoto, R. S., Blackfield, D. T., Fenstermacher, M. E., Bonoli, P. T., Porkolab, M., 16th European Conf. on Controlled Fusion and Plasma Physics, Venice, (European Physical Society, 1989) Vol. IV 1295.

[10] Freidberg, J. P. in "Ideal Magnetohydrodynamics" (Plenum, NY, 1987) Ch. 6, p. 111.

[11] Fuchs, V., Cairns, R. A., Shoucri, M. M., Hizanidis, K., Bers, A., Phys. Fluids 28 (1985) 3619.

[12] Bonoli, P. T., Ott, E., Phys. Fluids 25 (1982) 359.

[13] Furth, H. P., Rutherford, P., Selberg, H., Phys. Fluids 16 (1973) 1054.

[14] Hinton, F. L., Hazeltine, R. D., Rev. Mod. Phys. 48 (1976) 239.

[15] Grimm, R. C., Dewar, R. L., Manickam, J., Journal of Computational Physics 4 (1983) 94.

[16] Manickam, J., Pomphrey, N., Todd, A. M. M., Nucl. Fusion 27 (1987) 1461.

[17] Ramos, J. J., Phys. Rev. Lett. 60 (1988) 523.

Figure Captions

Fig. 1. RF power spectrum given by Eq. (3) with $S_A=1.0$, $n_A=3.0$, $\Delta n_A=1.41$, $S_B=0.1$, $n_B=6.0$, and $\Delta n_B=1.0$

Fig. 2. Model results for single launcher configuration after tenth iteration ($z_o=25$ cm and $P_{LH}=250$ kW). (a) Current density vs. $\hat{\psi}$. (b) q vs. $\hat{\psi}$ for $P_{LH} = 250$ kW (solid line) and for comparison $P_{LH} = 0$ (dash line).

Fig. 3. Model results for single launcher configuration after tenth iteration ($z_o=25$ cm and $P_{LH}=250$ kW). (a) Poloidal projection of ray trajectory ($n_{\parallel}^o=3.0$). (b) Electron distribution function vs. parallel kinetic energy on a flux surface ($\hat{\psi} \simeq 0.28$) near the maximum of the RF deposition profile.

Fig. 4. Model results for single launcher configuration after first iteration ($z_o=25$ cm and $P_{LH}=250$ kW). (a) Poloidal projection of ray trajectory ($n_{\parallel}^o=3.0$). (b) Current density vs. $\hat{\psi}$. (c) q vs. $\hat{\psi}$ for $P_{LH}=250$ kW (solid line) and for comparison $P_{LH}=0$ (dash line).

Fig. 5. Model results for single launcher configuration after tenth iteration, including bootstrap current generation ($z_o=25$ cm and $P_{LH} = 130$ kW). (a) Current density vs. $\hat{\psi}$. (b) q vs. $\hat{\psi}$ for $P_{LH} = 130$ kW (solid line) and for comparison $P_{LH}=0$ (dash line).

Fig. 6. Model results for multiple launcher configuration after tenth iteration, including bootstrap current generation [$z_o=(0, 12.5, 25)$ cm and $P_{LH} =(40, 40, 80)$ kW]. (a) Current density vs. $\hat{\psi}$. (b) q vs. $\hat{\psi}$ for $P_{LH}=160$ kW total (solid line) and for comparison $P_{LH}=0$ (dash line). (c) Poloidal projections of three ray trajectories with initial $n_{\parallel}^o=(5.0, 4.0, 3.0)$ for launch points of $z_o=(0, 12.5, 25)$ cm, respectively.
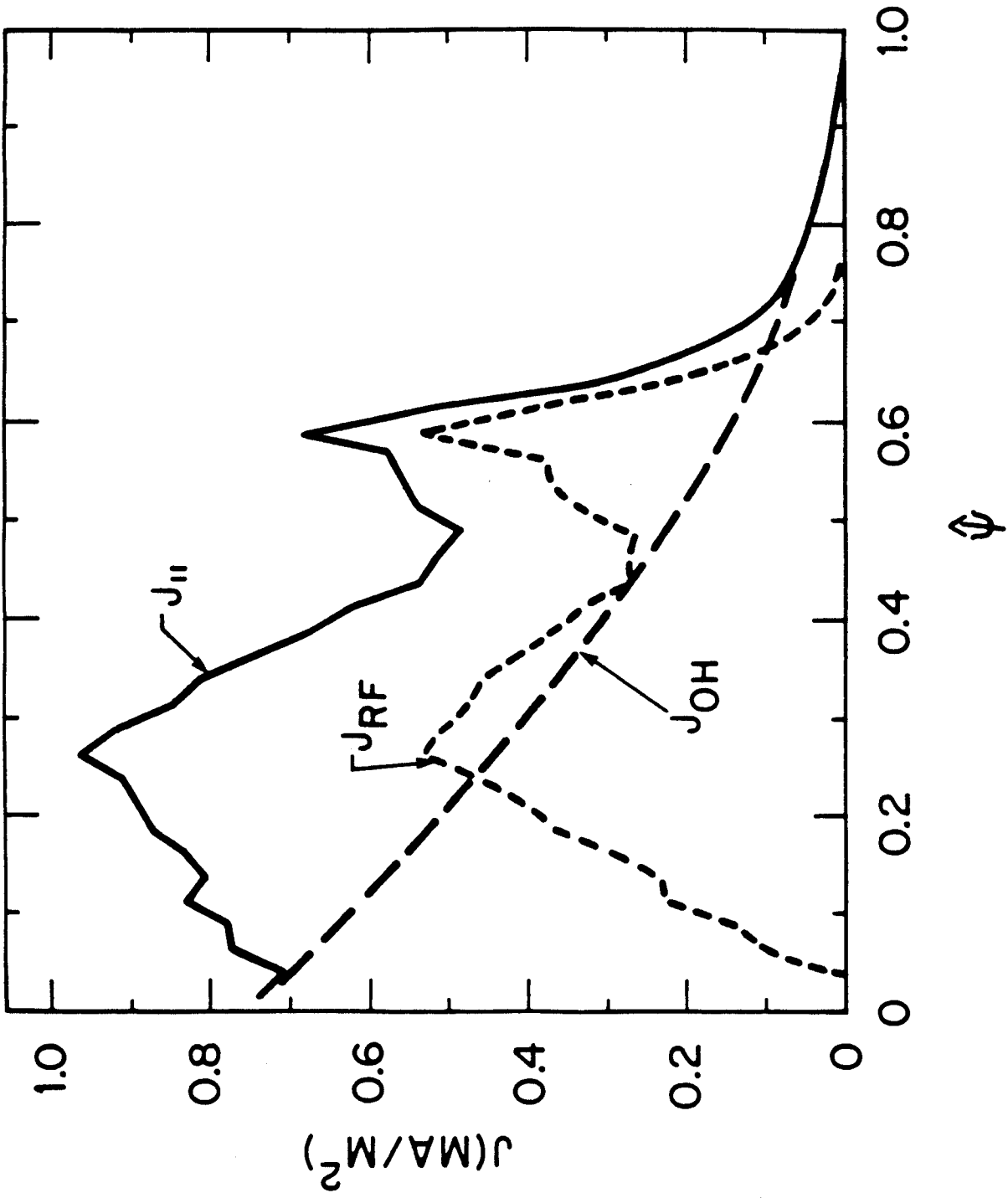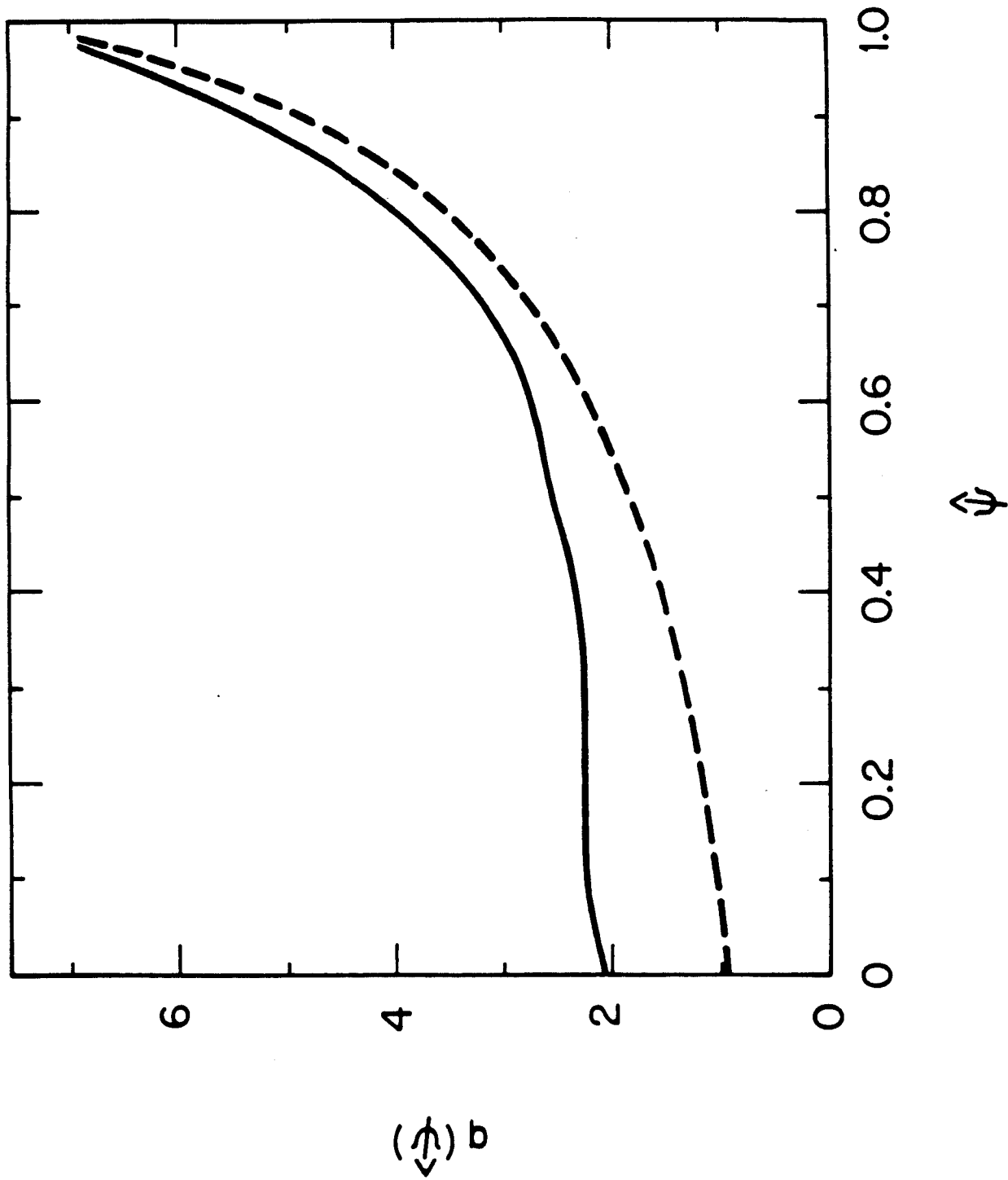
Figure 1

P (arb. units)

$n_{\parallel}$
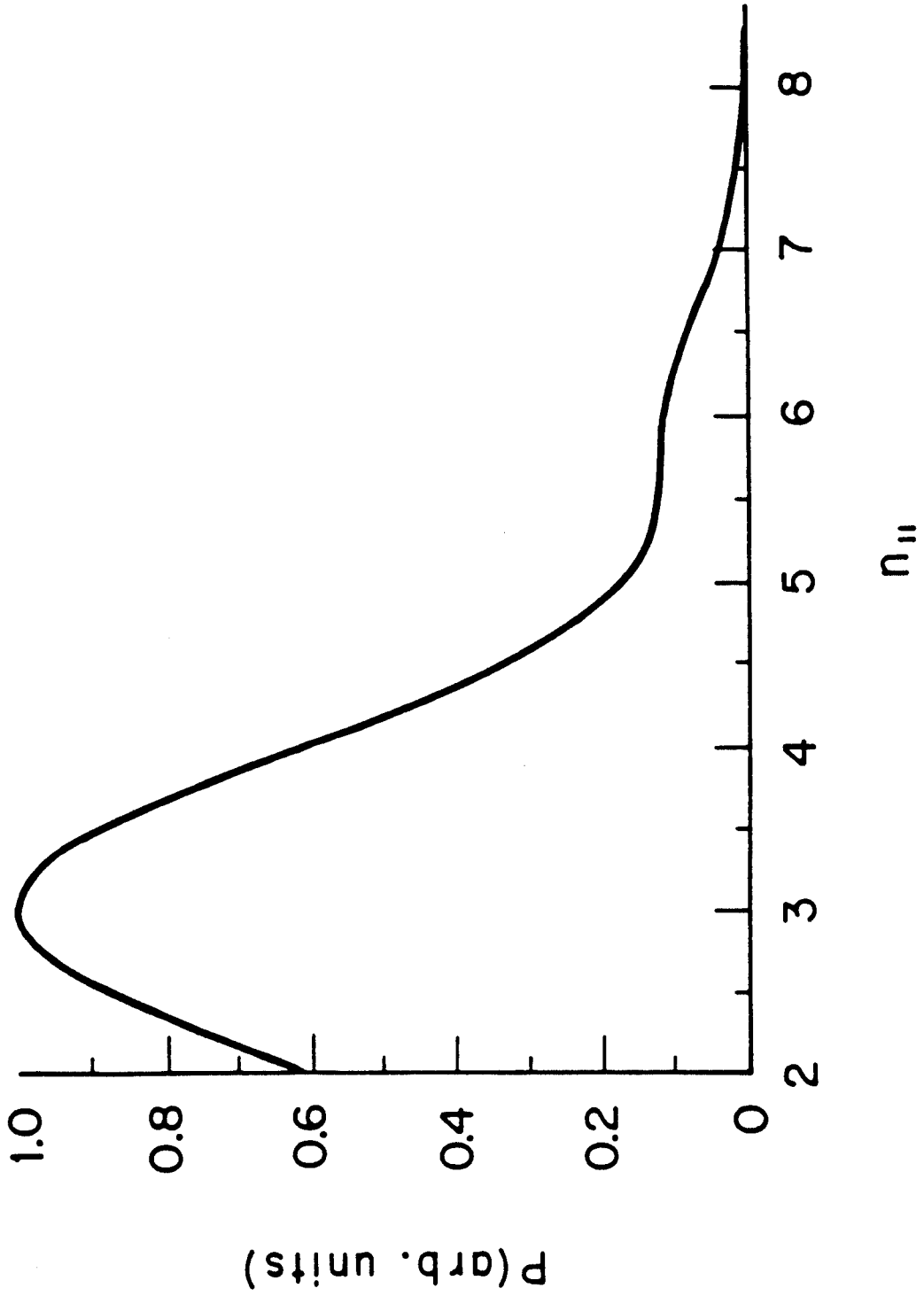
11

Figure 2(a)

Figure 2(b)

13
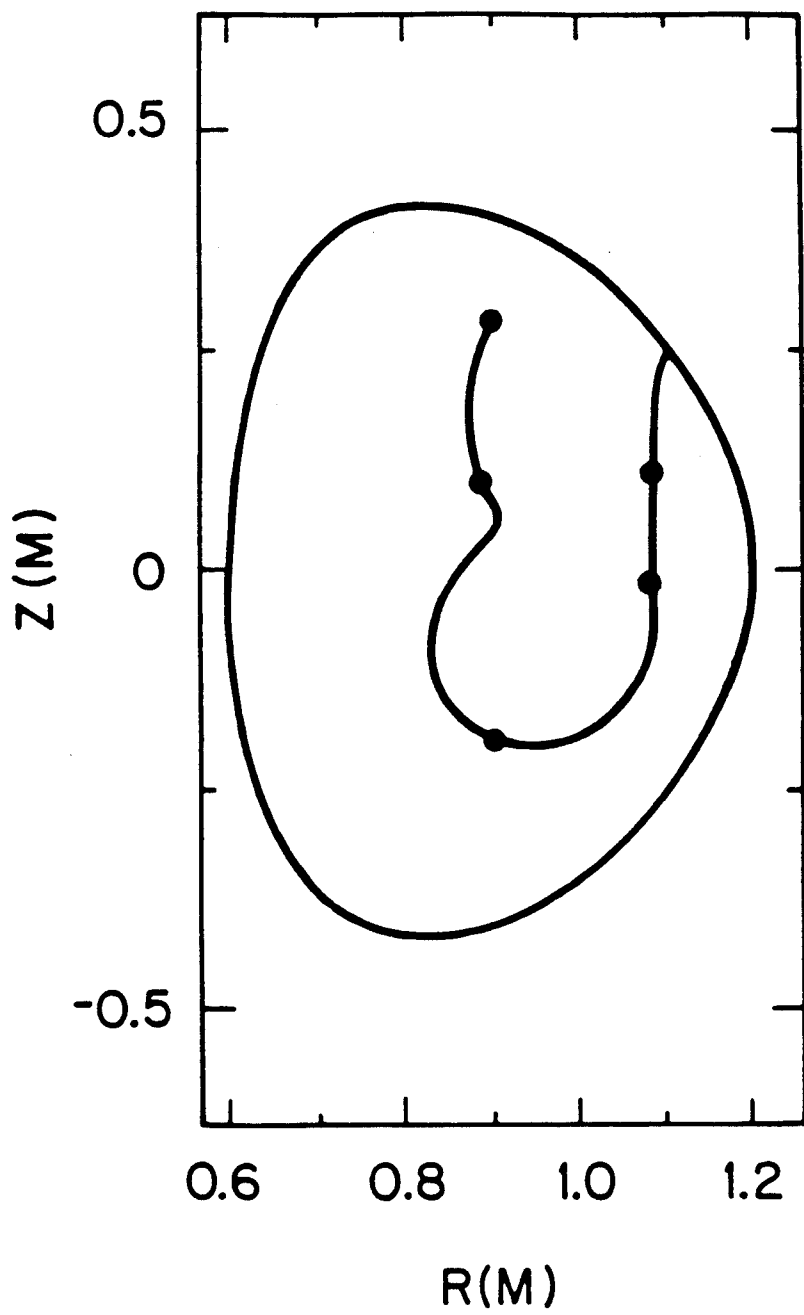
Figure 3(a)

Figure 3 (b)

15

Figure 4(a)

J(MA/M²)

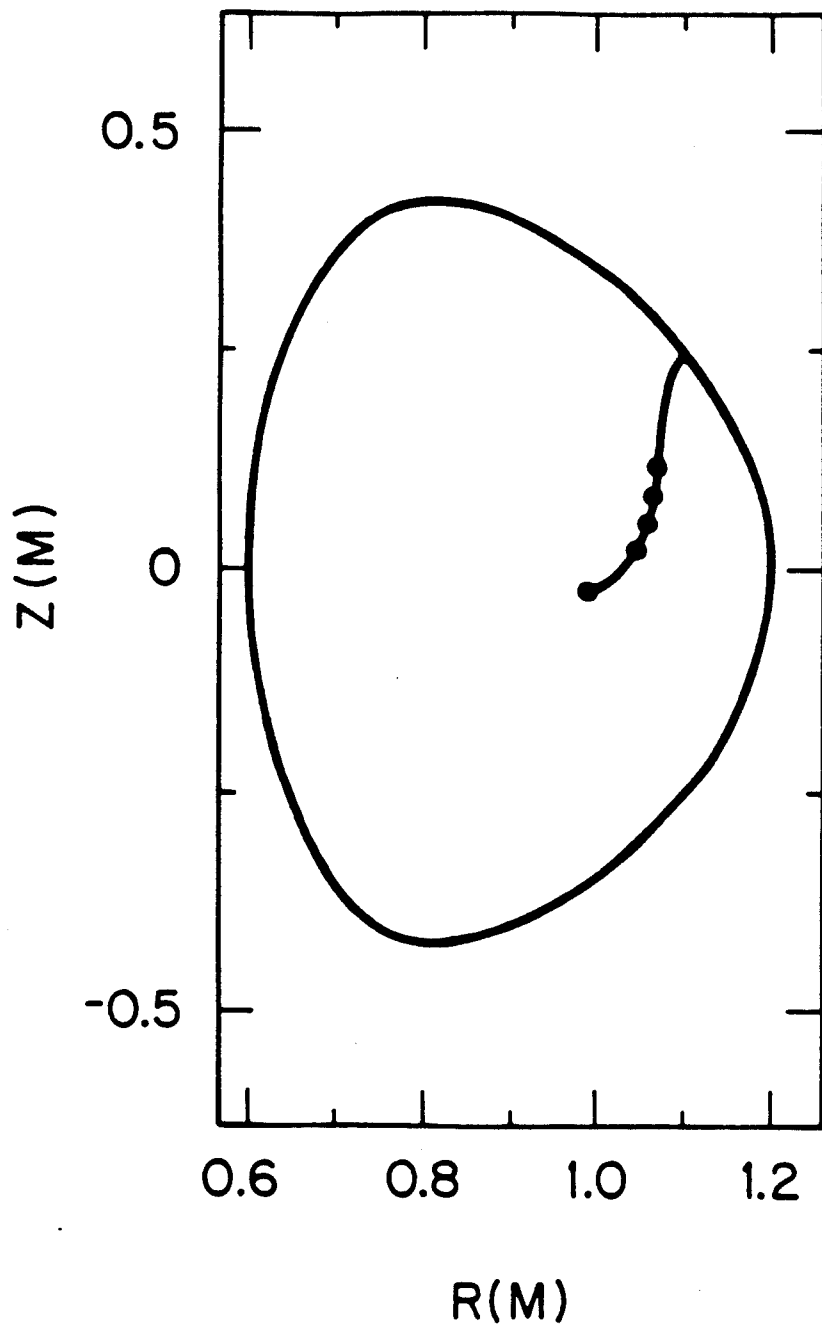$J_{||}$

J_{OH}

J_{RF}

$\hat{\psi}$
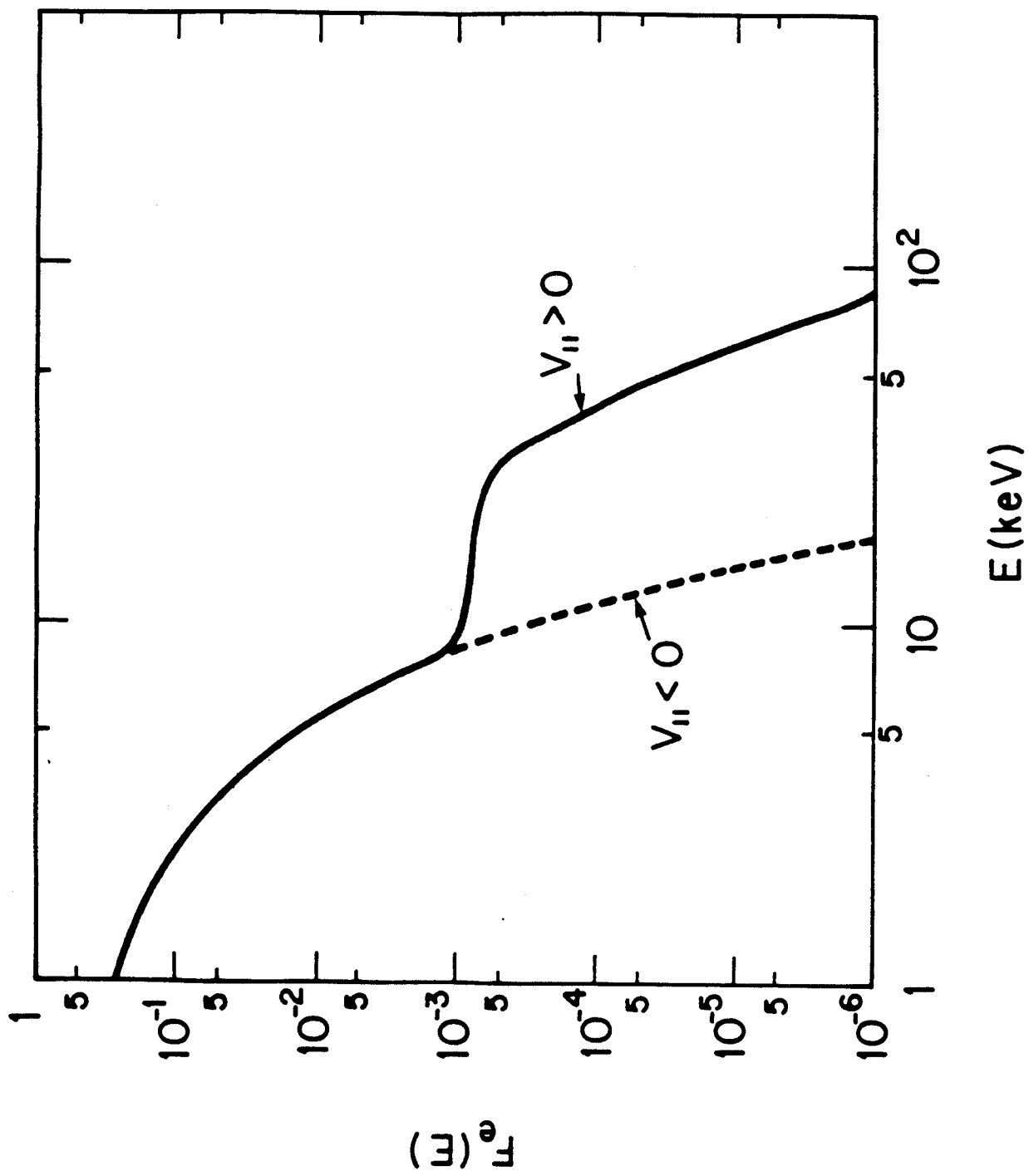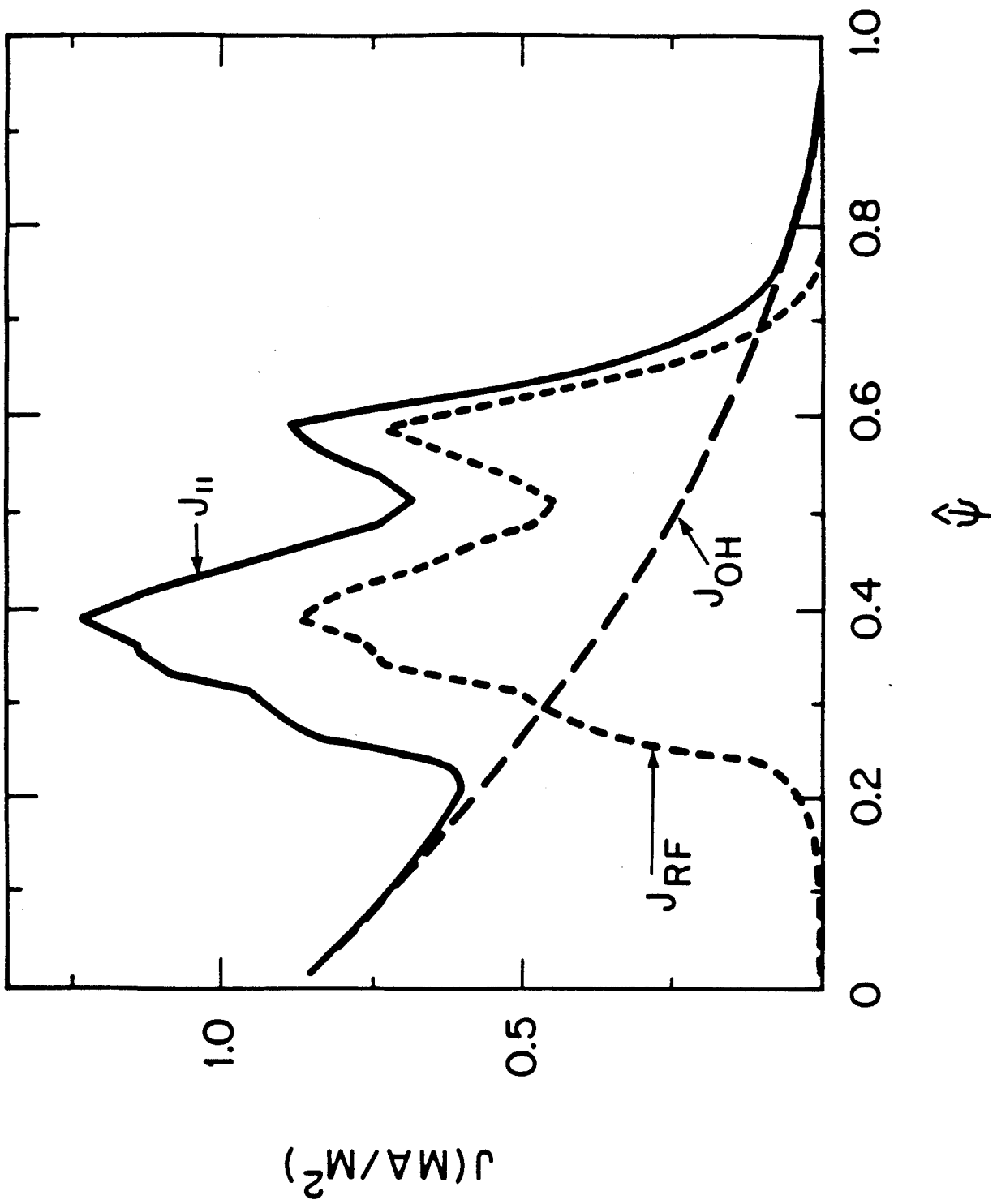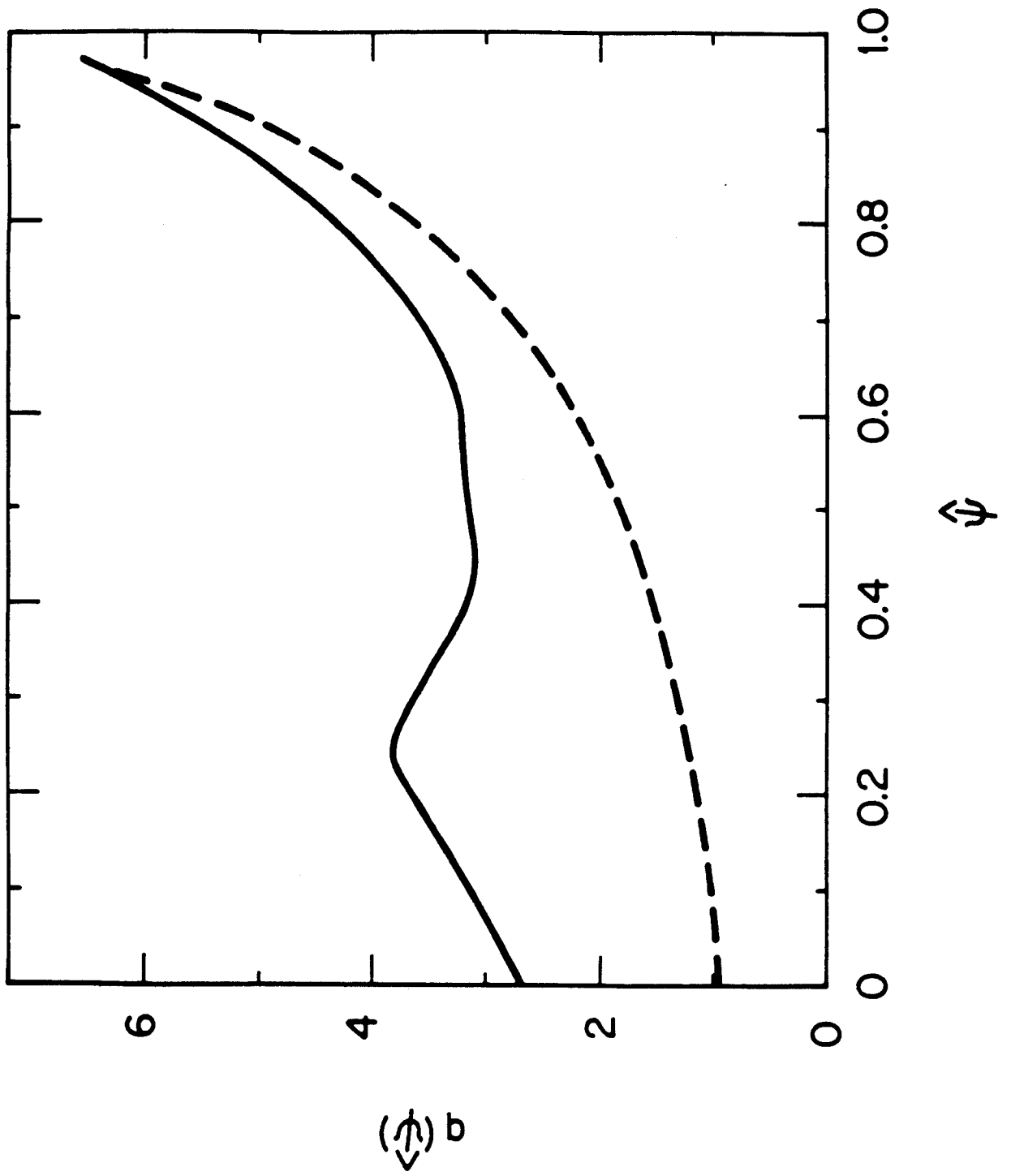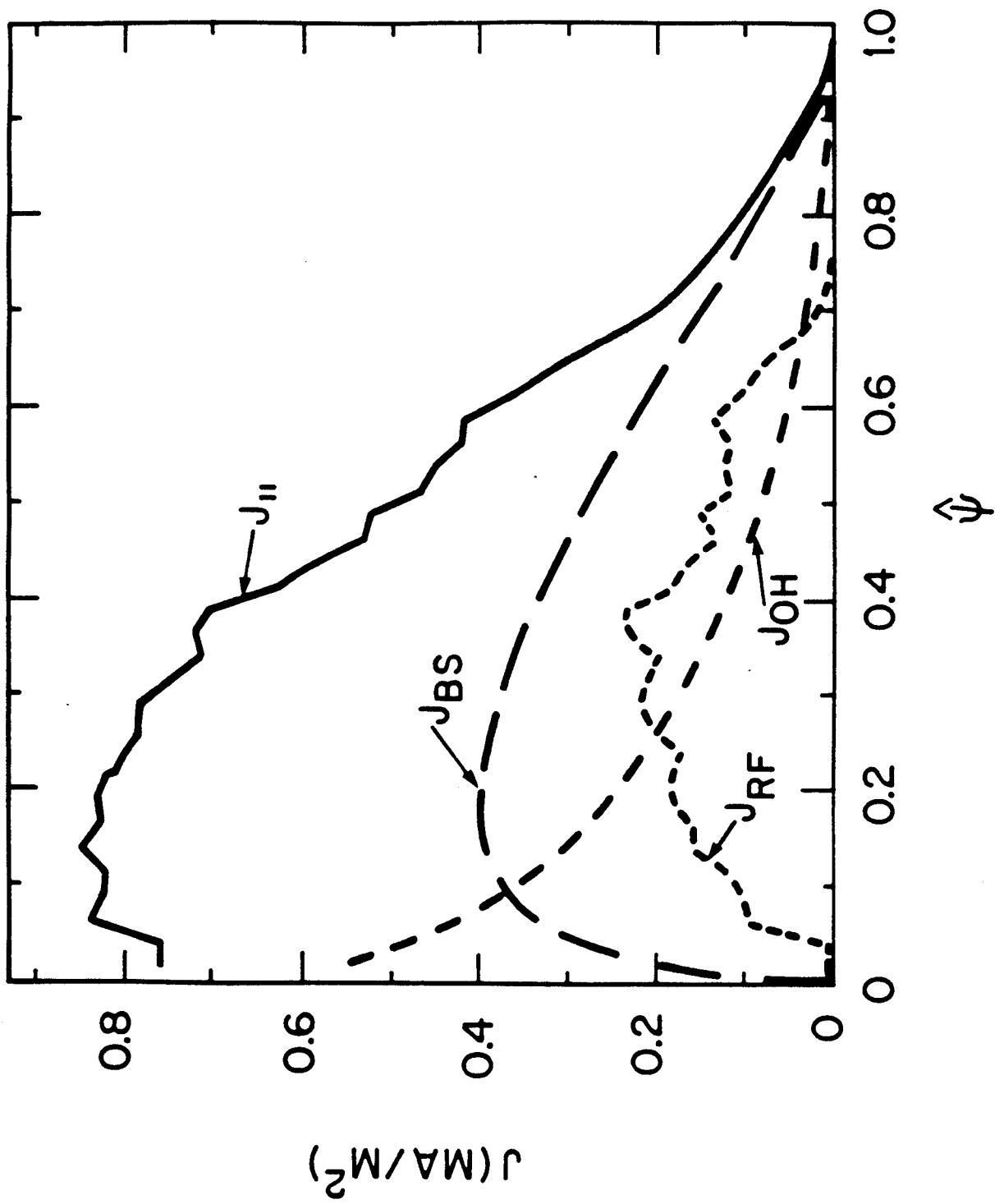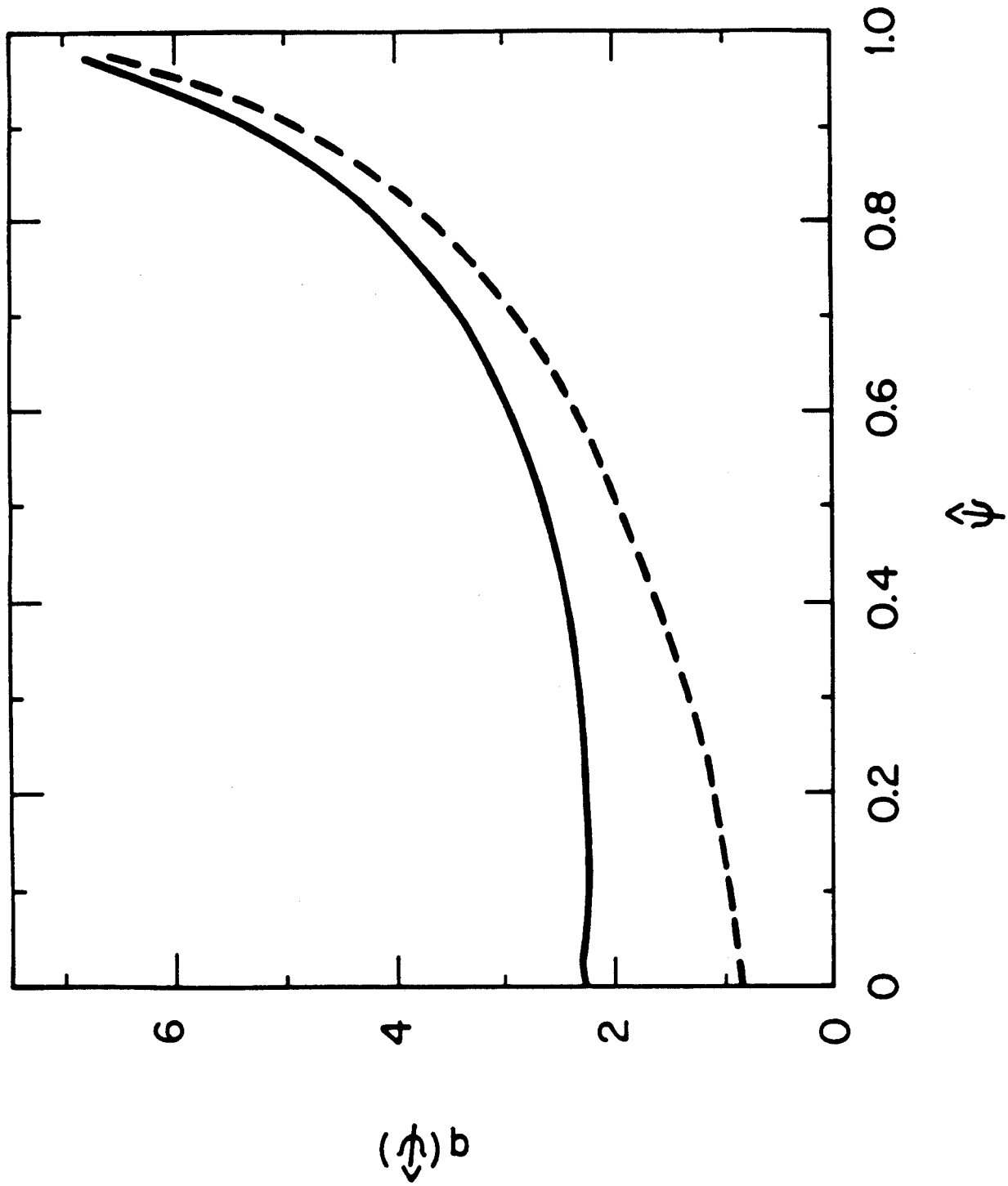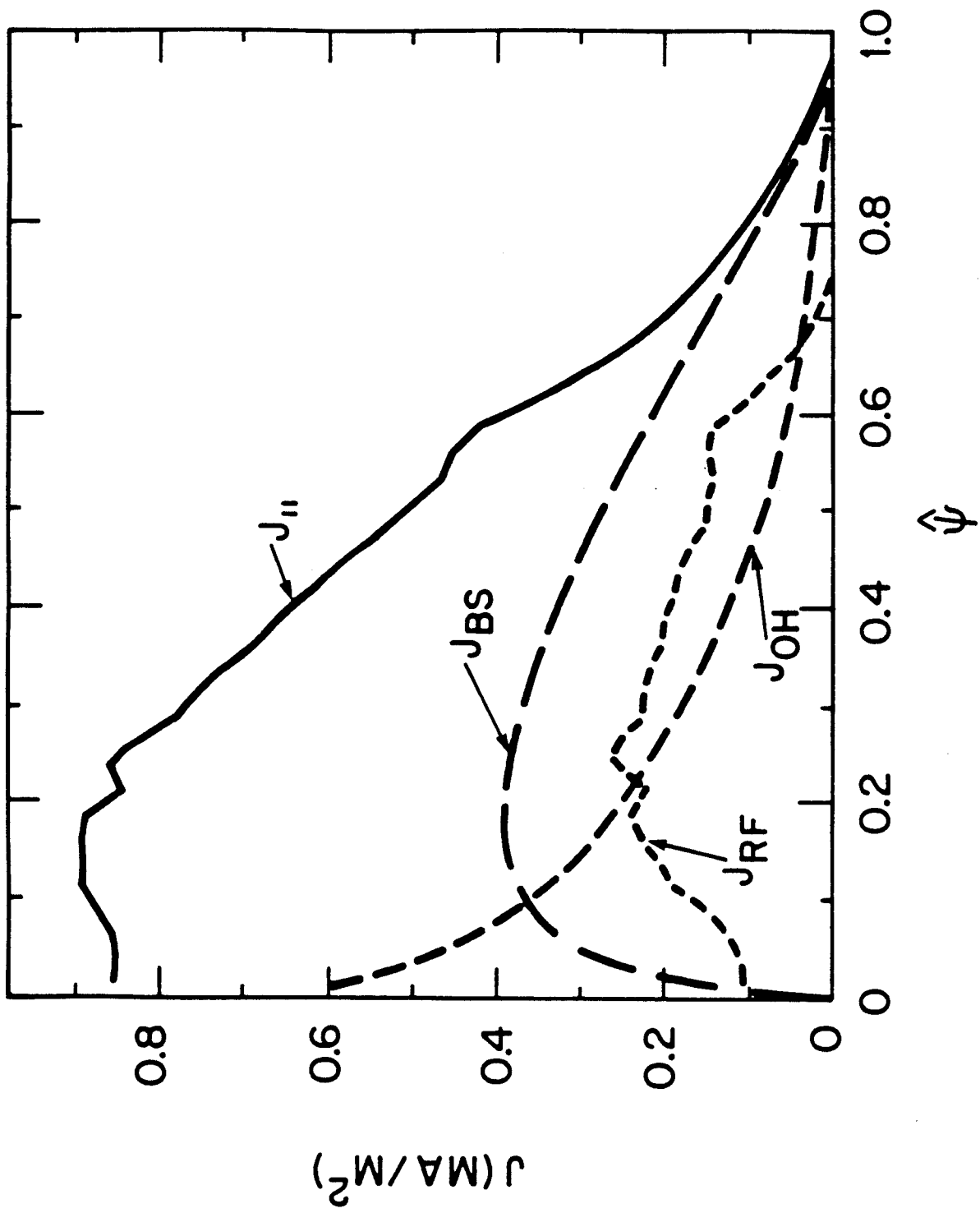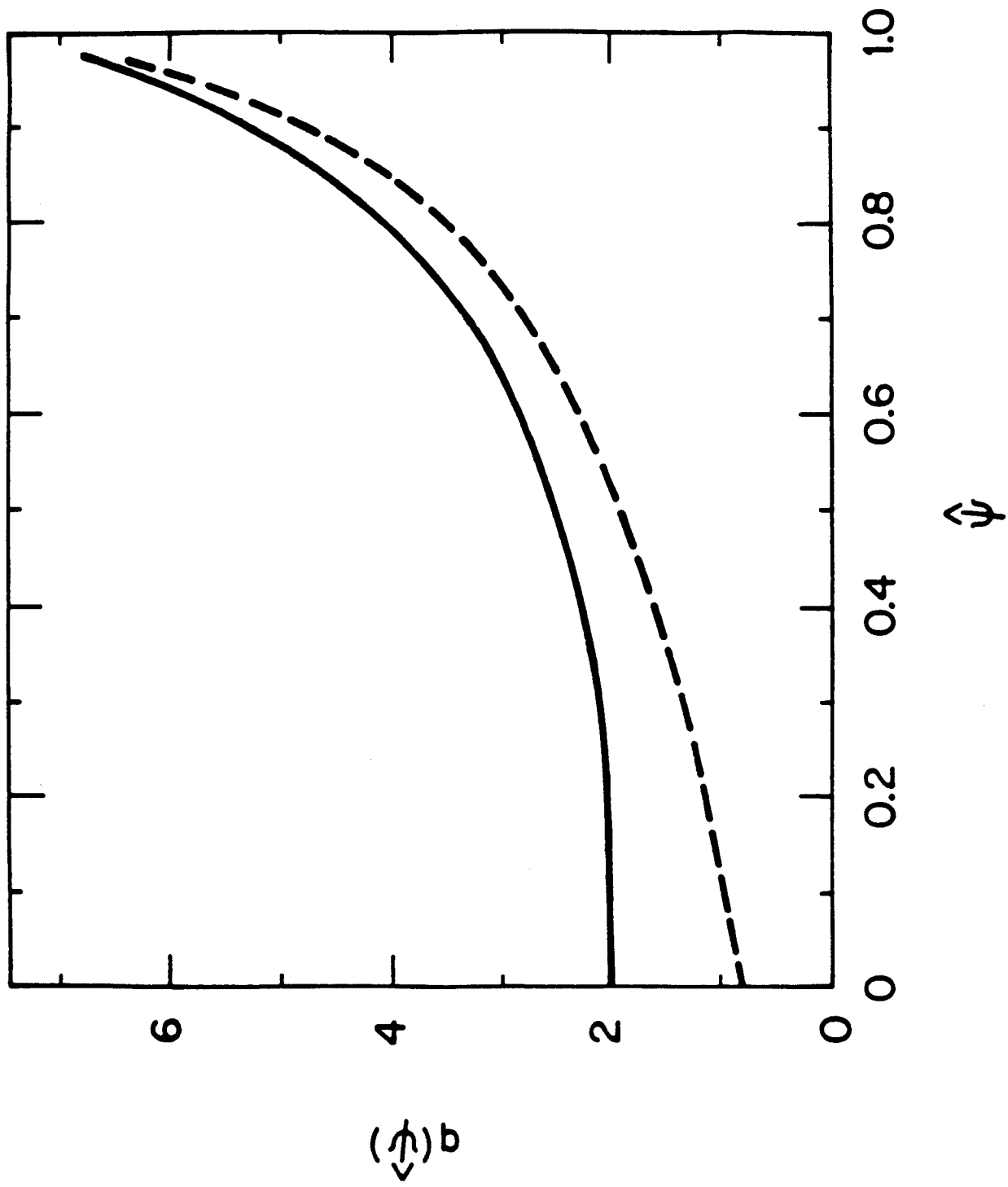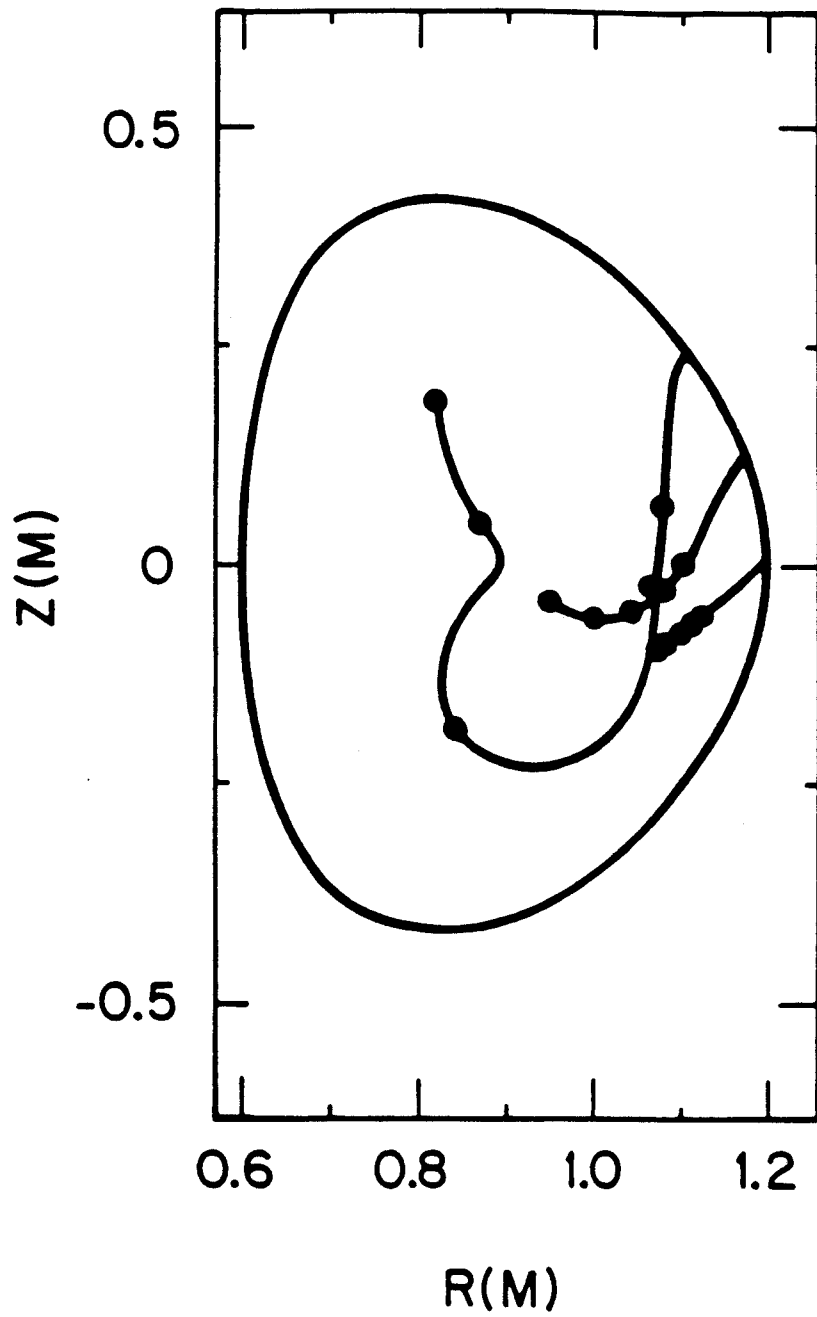
Figure 4(b)

Figure 4(c)

Figure 5(a)

Figure 5(b)

Figure 6(a)

Figure 6(b)

22

Figure 6(c)

23